







Machine learning via relativity-inspired quantum dynamics

Zejian Li , Valentin Heyraud , Kaelan Donatella , Zakari Denis , and Cristiano Ciuti 
Université Paris Cité, CNRS, Laboratoire Matériaux et Phénomènes Quantiques, 75013 Paris, France

 (Received 23 May 2022; revised 1 August 2022; accepted 8 August 2022; published 12 September 2022)

We present a machine-learning scheme based on the relativistic dynamics of a quantum system, namely a quantum detector inside a cavity resonator. An equivalent analog model can be realized for example in a circuit QED platform subject to properly modulated driving fields. We consider a reservoir-computing scheme where the input data are embedded in the modulation of the system (equivalent to the acceleration of the relativistic object) and the output data are obtained by linear combinations of measured observables. As an illustrative example, we have simulated such a relativistic quantum machine for a challenging classification task, showing a very large enhancement of the accuracy in the relativistic regime. Using kernel-machine theory, we show that in the relativistic regime the task-independent expressivity is dramatically magnified with respect to the Newtonian regime.

DOI: [10.1103/PhysRevA.106.032413](https://doi.org/10.1103/PhysRevA.106.032413)

I. INTRODUCTION

Among several approaches for the conception of quantum computing devices, the field of relativistic quantum information [1,2] has emerged. It has been demonstrated that noninertial motion, or, via the equivalence principle, gravitational fields, can be used to generate quantum gates. Recent theoretical works have demonstrated that a nonuniformly accelerated cavity can generate cluster states [3], two-mode squeezing [4], mode mixing [5], as well as other entangling gates [6] for continuous-variable quantum computing [7]. In a complementary scenario, a cavity remains inertial, but hosts accelerated detectors. Also for this configuration it has been shown that universal single-qubit rotations can be performed [8]. While all the existing proposals for relativistic quantum computing require a very challenging control of mechanical motion, the corresponding models can be however synthesized in artificial platforms [9–11] such as those based on circuit QED [12] or trapped ions [13].

In recent years, *reservoir computing* has emerged as an appealing paradigm of information processing [14]. This framework consists in approximating a target function by feeding its arguments as an input of a *reservoir*, the dynamics of which nonlinearly maps the data into a high-dimensional space. The resulting output data are then fed into a parametrized linear transformation to yield a trial function. These parameters are finally optimized through supervised learning. This architecture makes the computational resources involved in the training process relatively modest. This has led to proposals and realizations in diverse platforms, including free-space optics [15–17], photonics [18,19], nonlinear polariton lattices [20–22], memristors [23,24], and beyond [25–28]. Very recently, such an approach has been explored in a quantum context [29,30], with applications in quantum metrology [31,32], quantum-state control [33–35], and image recognition [36,37]. Although it was long thought that a

strong nonlinearity of the equations of motion was an essential element of reservoir computing, recent works have shown great performances relying on systems with almost no intrinsic nonlinearity, namely by exploiting the nonlinearity of the measurement [17,38,39] or drawing links with approximate kernel evaluation [40–42].

In this paper, we present a reservoir-computing scheme exploiting the relativistic motion of a quantum system. We consider a paradigmatic model describing a quantum detector (atom) moving inside a cavity resonator. The relativistic dynamics can be simulated by an analog system such as a circuit QED platform with a tailored modulation of driving fields [10]. We explore the dynamics where the input data are embedded into the system by modulating the acceleration of the detector and measured output observables are then fed to a trainable linear classifier. By evaluating task-independent figures of merit, we demonstrate that the expressivity of our machine-learning protocol is dramatically enhanced in the relativistic regime. Moreover, we provide an illustrative example with a challenging classification task.

II. RELATIVISTIC QUANTUM MODEL

Let us consider the model describing a quantum harmonic detector with proper frequency Ω , minimally coupled to a quantum field $\hat{\phi}$ inside an optical cavity. In the interaction picture, the corresponding Hamiltonian takes the Unruh-DeWitt form [43,44] $\hat{H}(\tau) = \lambda \hat{m}(\tau) \hat{\phi}[x^\mu(\tau)]$, where τ is the proper time of the detector, λ is the coupling constant, and $\hat{m}(\tau) = \hat{b} e^{-i\Omega\tau} + \hat{b}^\dagger e^{i\Omega\tau}$ depends on the detector annihilation (creation) operator \hat{b} (\hat{b}^\dagger). Finally, $x^\mu(\tau) = (t(\tau), x(\tau))$ is the world line of the detector in the 1+1D Minkowski spacetime. We will adopt the metric $\eta_{\mu\nu} = \text{diag}(+1, -1)$ and natural units such that $\hbar = c = 1$. For a multimode cavity with

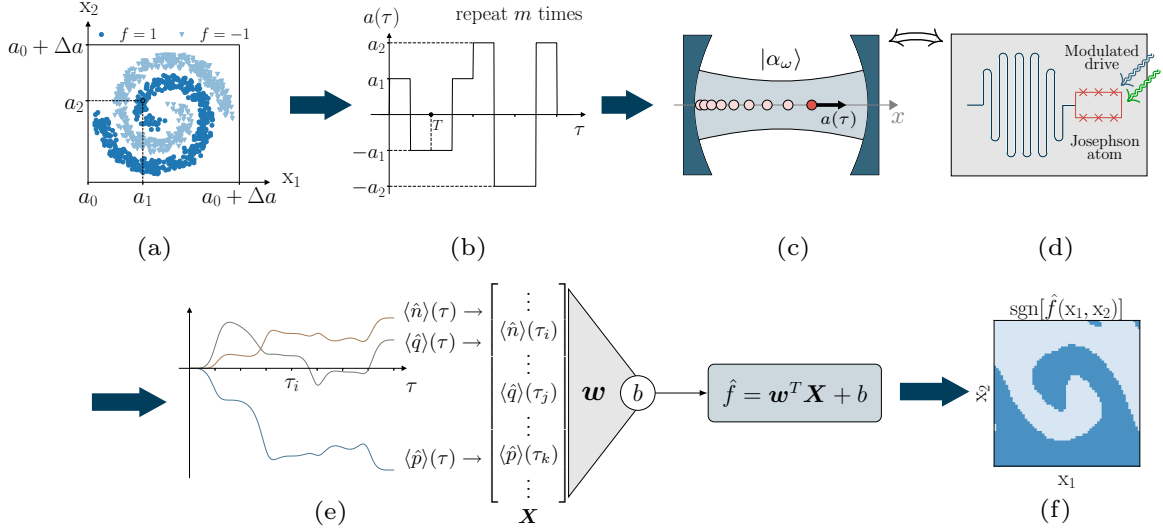


FIG. 1. Scheme of the relativistic reservoir-computing protocol. (a) Each point $\mathbf{x} = (x_1, x_2)$ of the dataset is linearly mapped to acceleration values (a_1, a_2) according to Eq. (5). (b) The acceleration values are used to construct a piecewise constant acceleration profile $a(\tau)$. (c) The quantum detector, initially at rest in the cavity prepared in a single-mode coherent state, undergoes noninertial motion with proper acceleration $a(\tau)$. (d) Analog circuit QED system where the analogous proper acceleration is controlled by modulated driving fields. (e) Observables of the detector are measured at different times giving the feature vector \mathbf{X} and the affine trial function $\hat{f} = \mathbf{w}^T \mathbf{X} + b$. (f) The classification result is predicted by $\text{sgn}[\hat{f}(x_1, x_2)]$.

perfectly reflecting mirrors [8,45],

$$\hat{H}(\tau) = \lambda \sum_{n=1}^{\infty} \frac{\sin[k_n x(\tau)]}{\sqrt{L\omega_n}} \times (\hat{b}\hat{a}_n e^{-i[\Omega\tau + \omega_n t(\tau)]} + \hat{b}\hat{a}_n^\dagger e^{-i[\Omega\tau - \omega_n t(\tau)]}) + \text{H.c.}, \quad (1)$$

where $\omega_n = k_n = n\pi/L$ and L is the cavity length. The mode operators (denoting $\hat{a}_0 \equiv \hat{b}$ for the detector) satisfy bosonic commutation relations $[\hat{a}_n, \hat{a}_m^\dagger] = \delta_{nm}$. Both rotating and counter-rotating terms are present and contribute in the noninertial regime [8,46–48].

Let us prepare the cavity in a single-mode coherent state $|\alpha_{\omega_i}\rangle$ [49] the frequency of which is resonant with that of the detector. Let us also consider the detector initially in its ground state $\hat{\rho}_{0,(a)} = |0_a\rangle\langle 0_a|$. The density matrix then reads

$$\hat{\rho}_0 = \hat{\rho}_{0,(a)} \otimes |\alpha_{\omega_i}\rangle\langle\alpha_{\omega_i}| \otimes \bigotimes_{j \neq i} |0_{\omega_j}\rangle\langle 0_{\omega_j}|. \quad (2)$$

For a given $x^\mu(\tau)$, the time evolution of the density matrix is given by

$$\frac{d\hat{\rho}(\tau)}{d\tau} = -i[\hat{H}(\tau), \hat{\rho}(\tau)]. \quad (3)$$

Since all the considered modes are bosonic and the Hamiltonian is quadratic, the Gaussianity of the initial state is preserved during the evolution. The dynamics of $\hat{\rho}(\tau)$ can therefore be solved exactly using the covariance-matrix formalism for Gaussian states [43,50–52] (see Appendix A).

III. CIRCUIT QED ANALOG IMPLEMENTATION

As shown in the literature [10], the Hamiltonian (1) can be implemented on a circuit QED platform consisting of an

artificial Josephson atom [53] coupled to a multimode transmission line resonator [see Fig. 1(d)] [10]. For a single mode, the Hamiltonian reads

$$\hat{H}^{\text{QED}}(\tau) = \omega_0 \hat{a}^\dagger \hat{a} + \epsilon \hat{b}^\dagger \hat{b} + \eta \zeta(\tau) \hat{b}^\dagger \hat{b} + g(\hat{b}^\dagger + \hat{b})(\hat{a}^\dagger + \hat{a}), \quad (4)$$

where ω_0 and ϵ are the bare frequencies of the transmission line resonator and the artificial atom respectively, and g is their coupling constant. $\zeta(\tau)$ is the sum of four driving fields containing two different tones and two nonadiabatically modulated phases (see Appendix C). To get the equivalent of the acceleration range considered in this paper, frequencies ω_0 and ϵ can be taken in the standard GHz range while g , Ω , and the phase modulation rates are in the MHz range (for more details, see Appendix C). This driving scheme gives rise to the same interaction-picture Hamiltonian as Eq. (1) for a single mode [54], and can be similarly extended to multimode circuit-QED systems [55–57]. While here we will report the results with a harmonic detector, we have also simulated the other extreme case where the Josephson atom is a *two-level system* and found similar results (see Appendix D), showing that the detailed atom spectrum is not crucial.

IV. RESERVOIR-COMPUTING PROTOCOL

The goal of supervised machine learning is to try to best approximate a (usually nonlinear) target function $y = f(\mathbf{x})$ of some input vector $\mathbf{x} \equiv (x_1, x_2, \dots, x_N)$ with a parametrized trial function $\hat{y} = \hat{f}(\mathbf{x})$ from a set of known example pairs. The input data are distributed according to some probability measure $\mu(d\mathbf{x})$, from which a restricted set of samples with their corresponding target values is known, $\{(\mathbf{x}_{(i)}, y_i)\}_i$. These are split into a training set of size N_{train} , that one exploits to optimize the trial function \hat{f} , and a testing set of size

N_{test} , used to assess the performance of the trained model. In this section, we will show in detail how one can harness the relativistic dynamics of the detector-cavity system to construct an expressive trial function \hat{f} within the paradigm of reservoir computing. In this framework, each input \mathbf{x} is first nonlinearly transformed by means of a physical system into an associated feature vector $\mathbf{X}(\mathbf{x})$, the components of which are then combined to yield the approximate output $\hat{f}(\mathbf{x})$ through a parametrized linear combination with trainable weights, to be optimized. Here, the above nonlinear embedding is obtained in a two-step procedure: (i) each input \mathbf{x} determines a specific world line of the detector, and (ii) a set of observables of the detector is measured to yield the feature vector $\mathbf{X}(\mathbf{x})$. This is schematically represented in Fig. 1.

Assuming that for every component x_i in the input vector \mathbf{x} we have $x_{i,\min} \leq x_i \leq x_{i,\max}$, we map them linearly to acceleration values in a fixed range between a_0 and $a_0 + \Delta a$, namely

$$x_i \mapsto a_i = a_0 + \Delta a \times \frac{x_i - x_{i,\min}}{x_{i,\max} - x_{i,\min}}. \quad (5)$$

We then impose a piecewise-constant proper acceleration [58] $a(\tau)$ to the harmonic detector. The pieces have proper acceleration values $(a_1, -a_1, -a_1, a_1, \dots, a_N, -a_N, -a_N, a_N)$ and each piece has a duration of $T/2$ in the proper frame of the detector, and we repeat this encoding sequence m times. Assuming the detector to be initially at rest at $x^\mu(\tau = 0) = (t = 0, x = 0)$, this acceleration profile guarantees that at each instant $\tau = nT$, $n \in \mathbb{N}$, the detector is at rest, and that at $\tau = 2nT$ it comes back to its original spatial position at $x = 0$. Note that for a circuit QED implementation the modulation of the driving fields can directly control the analog of the proper acceleration with respect to the proper time τ (see Appendix C). The detector world line for a general proper acceleration $a(\tau)$ is (see Appendix B for a derivation)

$$x(\tau) = \int_0^\tau d\tau' \sinh[\xi(\tau')], \quad t(\tau) = \int_0^\tau d\tau' \cosh[\xi(\tau')], \quad (6)$$

where $\xi(\tau) = \int_0^\tau d\tau' a(\tau')$ is the rapidity [59]. Instead, in the Newtonian case, the (unphysical) world line is simply

$$x_{\text{Newt}}(\tau) = \int_0^\tau d\tau' \xi(\tau'), \quad t_{\text{Newt}}(\tau) = \tau. \quad (7)$$

Each input data point \mathbf{x} determines a single time evolution of the system $\hat{\rho}(\tau)$. We can then measure the detector at times $\tau_n = n \times \Delta T$ to obtain the expectation values [60] of the quadrature operators $\hat{q} = (\hat{b} + \hat{b}^\dagger)/\sqrt{2}$, $\hat{p} = i(\hat{b}^\dagger - \hat{b})/\sqrt{2}$ and of the number operator $\hat{n} = \hat{b}^\dagger \hat{b}$. The measurements are then collected into a feature vector \mathbf{X} [61] [see Fig. 1(e)]. Finally, our trial function reads

$$\hat{f}(\mathbf{x}) = \mathbf{w}^T \mathbf{X}(\mathbf{x}) + b, \quad (8)$$

where the weight \mathbf{w} and bias b are parameters to be optimized in order for \hat{f} to approximate the target function f . To simplify the notation, in the following we will absorb b into the vector \mathbf{w} by appending a constant component 1 to the vector \mathbf{X} . Due to the linear dependence of the trial function on the feature vector, its optimization can be done analytically.

V. RESULTS AND DISCUSSION

As an illustrative example, we consider a nontrivial task: the two-spiral classification problem [62]. The goal is to distinguish two interlocking spiral planar patterns. This task serves as a well-known benchmark for binary pattern classification that is considered hard for multilayer perceptron models due to its complicated decision boundary [63]. The input data are the two coordinates of each point in the two-spiral pattern $\mathbf{x} = (x_1, x_2)$. The task function f to be learned is such that $f(\mathbf{x}) = 1$ if the point belongs to the first spiral branch, and $f(\mathbf{x}) = -1$ for the other branch [see Fig. 1(a)]. To train the model, we draw a train dataset of $N_{\text{train}} = 4000$ sample points $\{\mathbf{x}_{(1)}, \mathbf{x}_{(2)}, \dots, \mathbf{x}_{(N_{\text{train}})}\}$ with labels $y_i = f(\mathbf{x}_{(i)})$ and minimize the regularized least-square loss function. Although most classification problems are commonly treated with other losses [64], the training can be analytically performed under this choice of loss over the training set:

$$\mathcal{L}(\mathbf{w}) = \frac{1}{2N_{\text{train}}} \sum_{i=1}^{N_{\text{train}}} [y_i - \mathbf{w}^T \mathbf{X}(\mathbf{x}_{(i)})]^2 + \frac{l}{2} \|\mathbf{w}\|_2^2, \quad (9)$$

where the last term is a regularization term to prevent overfitting. Denoting Φ the matrix whose j th column is $\mathbf{X}(\mathbf{x}_{(j)})$, and \mathbf{y} the column vector of the training labels y_i , the optimal weights are given by $\mathbf{w}^* = (\Phi \Phi^T + lN_{\text{train}} \mathbb{1})^{-1} \Phi \mathbf{y}$. The performance of the model is then evaluated on a test sample with $N_{\text{test}} = 1000$ points. We evaluate the classification accuracy $\mathcal{A}_{\text{test}}$ on the test set as the fraction of correctly classified samples among N_{test} . The training accuracy $\mathcal{A}_{\text{train}}$, which indicates how well the reservoir-computing model fits the training set, is defined analogously. The transformation of the input $\mathbf{x} \mapsto \mathbf{X}(\mathbf{x})$ can be regarded as an embedding of the input from input space into some higher-dimensional feature space. This is best understood by introducing the kernel function [64] $k(\mathbf{x}, \mathbf{x}') = [\mathbf{X}(\mathbf{x}')^T \mathbf{X}(\mathbf{x})]$. Under quite general assumptions, this kernel can be diagonalized into an orthonormal [65] set of eigenfunctions $\{\psi_i\}_i$ with positive eigenvalues $\{\gamma_i\}_i$ [66]:

$$k(\mathbf{x}, \mathbf{x}') = \sum_i \gamma_i \psi_i(\mathbf{x}) \psi_i(\mathbf{x}'). \quad (10)$$

The set $\{\psi_i\}_i$ can be completed to be a basis of L_μ^2 [67] with eigenfunctions associated with $\gamma_i = 0$. Note that the kernel spectrum can be empirically computed [68] by calculating the eigenvalues of the matrix $\Phi \Phi^T / N_{\text{train}}$. The trial function of Eq. (8) may be rewritten in the above kernel eigenbasis as $\hat{f}(\mathbf{x}) = \boldsymbol{\beta}^T \boldsymbol{\psi}(\mathbf{x})$ where $\boldsymbol{\beta}$ is the weight vector to be optimized. The spectrum of the kernel contains crucial information as eigenfunctions with vanishingly small associated eigenvalues do not contribute to the expressivity of the reservoir [42]. In what follows, we will use the kernel spectrum to assess the expressivity of the model.

Throughout our simulations, we fixed the coupling constant to $\lambda = 0.1$, the interval of measurement to $\Delta T = T/2$, and $\Delta a/a_0 = 0.1$. The detector's proper frequency is set to be resonant with the third cavity mode [69] $\Omega = \omega_3$, the latter being initially in a coherent state $|\alpha\rangle$ with $\alpha = 10i$. We express all quantities in natural units with the scale fixed by Ω . The regularization is set to $l = 10^{-6}$; this is equivalent to having a measurement noise of variance l in the observables [70].

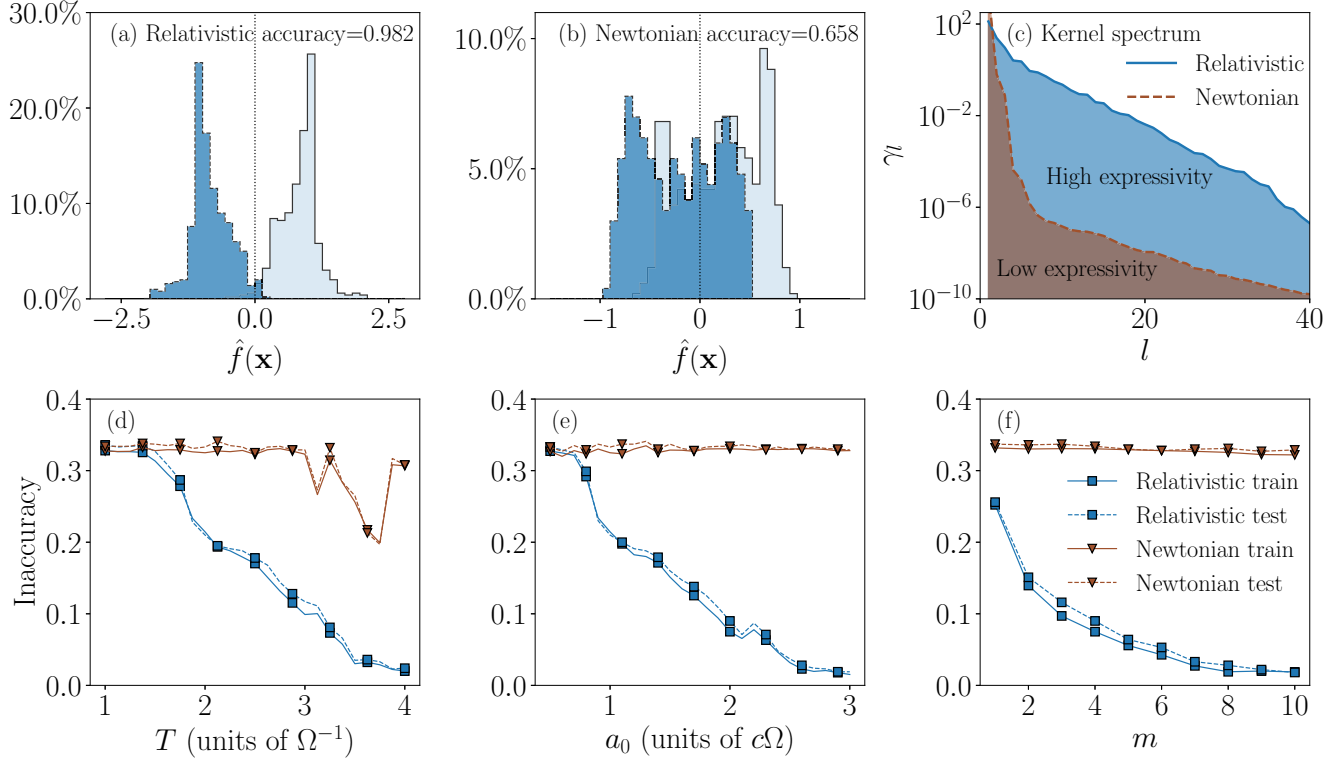


FIG. 2. Figures of merit of the relativistic reservoir-computing protocol. (a) Light and dark histograms correspond to testing samples belonging to different spirals of the dataset. Parameters: $a_0 = 3$, $T = 2$, and $m = 4$. (b) Same quantity plotted for the Newtonian model with same parameters. (c) The empirical kernel spectrum computed for the relativistic (solid line) and Newtonian (dashed line) models with same parameters. The first 40 nonzero eigenvalues γ_l are plotted in descending order. (d) Inaccuracy of the relativistic (triangles) and Newtonian (squares) models evaluated on both the training (solid lines) and testing (dashed lines) set, as a function of the acceleration time T . Parameters: $a_0 = 1$ and $m = 4$. (e) Same quantities plotted as a function of the base acceleration a_0 , for $T = 2$ and $m = 4$. (f) Same quantities plotted as a function of the number of repetitions m , for $a_0 = 2$ and $T = 2$. Quantities are expressed in natural units, where the scale is fixed by the proper frequency of the atom Ω .

Figure 2(a) shows the distribution of testing samples in feature space, represented by $\hat{f}(\mathbf{x})$. The same quantities are plotted in Fig. 2(b) in a nonrelativistic setting, that is, considering Newtonian world lines [Eq. (7)]. As appears from Figs. 2(a) and 2(b), the relativistic model correctly separates the two classes with high accuracy. By contrast, the system undergoing Newtonian dynamics exhibits a poor performance. The empirical kernel spectra of the two models are plotted in Fig. 2(c), where we show the first 40 nonzero eigenvalues γ_l in descending order. The flatter distribution of the relativistic kernel spectrum implies that for a fixed cutoff threshold on the eigenvalues (or a fixed regularization [42]), it has more eigenfunctions with nonzero eigenvalues that can contribute to the expressivity of the trial function \hat{f} in comparison with the Newtonian model. Importantly, this relativistically enhanced kernel expressivity associated to the dynamics is *task independent* and explains the much higher accuracy achieved by the relativistic model for the specific two-spiral classification task.

In Fig. 2(d), we examine the impact of the acceleration time T on the performance of the model. As T increases, the inaccuracy ($1 - \mathcal{A}$) of the relativistic model decreases to around zero, whereas the performance of the Newtonian model remains poor. This is consistent with the results of Fig. 2(e), where we vary the base acceleration a_0 for fixed T . Therein, we also found the inaccuracy of the relativistic model

to be decreasing as a function of a_0 as the motion enters the relativistic regime, and a poor performance of the Newtonian model, which remains insensitive to a_0 .

In Fig. 2(f) we study the effect of the number of repetitions m of the encoding sequence on the performance. As we are taking measurements at a constant interval ΔT , a larger value of m allows for more features to be collected in the feature vector X , improving the efficiency. By contrast, in the Newtonian setting, the supplementary features are close-to-linearly related to the previous ones, thus yielding a negligible improvement. The induced nonlinearity of the feature map associated to the dynamics of the relativistic reservoir ensures that the generated features remain nontrivial after many repetitions. The advantage of the relativistic model can be understood from Eq. (1). Indeed, as discussed in [8], the phases $e^{-i[\Omega\tau \pm \omega_n t(\tau)]}$ depend nontrivially on τ due to the relativistic (time-dilation) effects, which yields an input-dependent modulation of the cavity-detector resonance condition, absent in the Newtonian model, where one always has $t_{\text{Newt}}(\tau) = \tau$.

VI. CONCLUSIONS

We have shown how relativistic quantum dynamics can provide a dramatic enhancement of the expressive power for

reservoir computing. Given that analogs of the considered relativistic quantum model can be implemented in state-of-the-art quantum platforms, such as superconducting circuits and trapped ions, our theoretical findings pave the way to relativity-inspired machine-learning protocols with enhanced capabilities.

ACKNOWLEDGMENTS

We acknowledge support by the FET FLAGSHIP Project PhoQuS (Grant No. ID: 820392) and by the French Projects NOMOS (Grant No. ANR-18-CE24-0026) and TRIANGLE (Grant No. ANR-20-CE47-0011). We also thank the Ile de France region via the program SIRTEQ. This work was granted access to the HPC resources of TGCC under Grant No. A0100512462 attributed by Grand Equipement National de Calcul Intensif.

APPENDIX A: GAUSSIAN FORMALISM FOR THE MODEL WITH A HARMONIC DETECTOR

We briefly summarize the Gaussian formalism adopted for calculating the time evolution of the relativistic quantum system. We denote the vector of bosonic mode operators by

$$\hat{\Psi} = (\hat{a}_0, \hat{a}_1, \hat{a}_2, \dots, \hat{a}_N, \hat{a}_0^\dagger, \hat{a}_1^\dagger, \hat{a}_2^\dagger, \dots, \hat{a}_N^\dagger)^T, \quad (\text{A1})$$

that satisfies the commutation relation

$$[\hat{\Psi}_i, \hat{\Psi}_j] = \Omega_{ij}, \quad (\text{A2})$$

where

$$\Omega = \begin{bmatrix} \mathbf{0} & \mathbb{1} \\ -\mathbb{1} & \mathbf{0} \end{bmatrix} = -\Omega^T \quad (\text{A3})$$

is the symplectic form. If the Hamiltonian can be written in the form of

$$\hat{H} = \hat{\Psi}^T \mathbf{F}(t) \hat{\Psi}, \quad (\text{A4})$$

it then preserves the Gaussianity of states [50]. The Heisenberg equations of motion can be written as

$$\frac{d}{dt} \hat{\Psi} = -i\Omega \mathbf{F}^{\text{sym}}(t) \hat{\Psi}, \quad (\text{A5})$$

where $\mathbf{F}^{\text{sym}} = \mathbf{F} + \mathbf{F}^T$.

If we define the propagator $\mathbf{S}(t)$ via the relation

$$\hat{\Psi}(t) = \mathbf{S}(t) \hat{\Psi}(0), \quad (\text{A6})$$

it then satisfies the first-order linear differential equation

$$\frac{d}{dt} \mathbf{S}(t) = -i\Omega \mathbf{F}^{\text{sym}}(t) \mathbf{S}(t) \quad (\text{A7})$$

with the initial condition $\mathbf{S}(0) = \mathbb{1}$. The evolution of the covariance matrix

$$\sigma_{ij} = \langle \hat{\Psi}_i \hat{\Psi}_j \rangle - \langle \hat{\Psi}_i \rangle \langle \hat{\Psi}_j \rangle \quad (\text{A8})$$

is given by

$$\sigma(t) = \mathbf{S}(t) \sigma(0) \mathbf{S}^T. \quad (\text{A9})$$

σ together with $\langle \hat{\Psi} \rangle$ will completely specify a Gaussian state.

APPENDIX B: DERIVATION OF THE WORLD LINE

We derive here the world line for an observer with time-dependent proper acceleration $a(\tau)$ in 1 + 1D Minkowski spacetime with metric $\eta_{\mu\nu} = \text{diag}(+1, -1)$.

We parametrize the world line by the proper time $x^\mu(\tau) = (t(\tau), x(\tau))$ and denote

$$\begin{aligned} u^\mu(\tau) &= \frac{d}{d\tau} x^\mu(\tau) = (u^t(\tau), u^x(\tau)), \\ a^\mu(\tau) &= \frac{d}{d\tau} u^\mu(\tau) = (a^t(\tau), a^x(\tau)). \end{aligned} \quad (\text{B1})$$

From the definition of these quantities, we get

$$\begin{aligned} u^\mu u_\mu &= 1 = (u^t)^2 - (u^x)^2, \\ a^\mu u_\mu &= 0 = a^t u^t - a^x u^x, \\ a^\mu a_\mu &= -a(\tau)^2 = (a^t)^2 - (a^x)^2. \end{aligned} \quad (\text{B2})$$

It follows that

$$a^x = \frac{du^x}{d\tau} = a(\tau) \sqrt{1 + (u^x)^2}. \quad (\text{B3})$$

Integrating from $\tau' = 0$ to $\tau' = \tau$ gives

$$\begin{aligned} u^x(\tau) &= \sinh[\xi(\tau)], \\ \xi(\tau) &= \sinh^{-1}[u^x(\tau = 0)] + \int_0^\tau d\tau' a(\tau'). \end{aligned} \quad (\text{B4})$$

Integrating again gives the position. For the time, a similar treatment applies. We finally obtain

$$\begin{aligned} x(\tau) &= x_0 + \int_0^\tau d\tau' \sinh[\xi(\tau')], \\ t(\tau) &= t_0 + \int_0^\tau d\tau' \cosh[\xi(\tau')], \end{aligned} \quad (\text{B5})$$

which reduces to the world line equations in the main text for an observer initially at rest. Note that for a constant acceleration, this gives the well-known Rindler observer's world line.

APPENDIX C: IMPLEMENTATION WITH CIRCUIT QED

We present a potential implementation of the proposed relativistic model on circuit QED platforms inspired by [10], which consists of a Josephson artificial atom with bosonic mode operator \hat{b} (simulating the harmonic oscillator described in the main text) coupled to a microwave cavity in the strong-coupling regime. Denoting the microwave cavity mode operator by \hat{a} , the noninteracting Hamiltonian of the system is

$$\hat{H}_0(\tau) = \omega_0 \hat{a}^\dagger \hat{a} + \epsilon \hat{b}^\dagger \hat{b} + \eta \zeta(\tau) \hat{b}^\dagger \hat{b}, \quad (\text{C1})$$

where ω_0 is the cavity bare frequency, ϵ is the energy of the artificial atom, and we assumed that the Josephson junction has negligible nonlinearity. This can be achieved for example by replacing a single Josephson junction with a sufficiently long chain of junctions. The opposite extreme case, where the Josephson atom is a two-level system (qubit), yields similar results, as revealed by corresponding simulations reported in Appendix D. $\zeta(\tau)$ is a driving function that takes the follow-

ing form [71]:

$$\zeta(\tau) = \frac{d}{d\tau} F(\tau), \quad F(\tau) = F_+(\tau) + F_-(\tau), \quad (\text{C2})$$

where

$$F_{\pm} = \cos[\omega_{\pm}\tau \mp \theta_{\mp}(\tau)] - \cos[\omega_{\pm}\tau \mp \theta_{\pm}(\tau)]. \quad (\text{C3})$$

Assuming that the phases $\theta_{\pm}(\tau)$ are modulated slowly compared to the driving frequencies ω_{\pm} , as will indeed be the case in what follows, the driving function $\zeta(\tau)$ can be well approximated by

$$\begin{aligned} \zeta(\tau) \simeq & -\omega_+ \sin[\omega_+\tau - \theta_-(\tau)] \\ & + \omega_+ \sin[\omega_+\tau - \theta_+(\tau)] \\ & - \omega_- \sin[\omega_-\tau + \theta_+(\tau)] \\ & + \omega_- \sin[\omega_-\tau + \theta_-(\tau)]. \end{aligned} \quad (\text{C4})$$

The interaction Hamiltonian in the Schrödinger picture is $\hat{H}_I = g(\hat{b}^\dagger + \hat{b})(\hat{a} + \hat{a}^\dagger)$. Passing to the interaction picture with respect to $\hat{H}_0(\tau)$ and assuming $\eta \ll 1$ in the driving term, we get

$$\begin{aligned} \hat{H}_I(\tau) &= g[\hat{b}^\dagger e^{i\epsilon\tau} \mathcal{G}(\tau) + \text{H.c.}](\hat{a}e^{-i\omega_0\tau} + \text{H.c.}), \\ \mathcal{G}(\tau) &= e^{i\eta F(\tau)} \simeq 1 + i\eta F(\tau). \end{aligned} \quad (\text{C5})$$

To simulate a harmonic oscillator with proper frequency Ω and world line $x^\mu(\tau) = (t(\tau), x(\tau))$ coupled to the n th mode of a massless scalar field of frequency $\omega_n = k_n$ as considered in the main text, we now choose $\omega_{\pm} = \epsilon \pm \omega_0 - \Omega$ as the driving frequencies and $\theta_{\pm}(\tau) = \omega_n t(\tau) \pm k_n x(\tau)$ as the phase modulations. In the regime where $\epsilon, \omega_0, |\epsilon \pm \omega_0| \gg g$, the interaction Hamiltonian becomes (keeping only slowly rotating terms)

$$\begin{aligned} \hat{H}_I(\tau) &\simeq g\eta \sin[k_n x(\tau)] \\ &\times \hat{b}(\hat{a}e^{-i[\Omega\tau + \omega_n t(\tau)]} + \hat{a}^\dagger e^{-i[\Omega\tau - \omega_n t(\tau)]}) + \text{H.c.}, \end{aligned} \quad (\text{C6})$$

which takes the form of the interaction Hamiltonian in the main text for a single mode of the quantum field. Note that since we always consider a single-mode coherent state as the field initial state in the main text, the main contribution to the dynamics of the harmonic oscillator comes uniquely from this mode, as one can verify using perturbation theory [8]. We also checked numerically that a single-mode approximation for the quantum field is enough for obtaining accurate results for the simulations presented in the main text. Nonetheless, it is possible to simulate the full many-mode Hamiltonian by using multiple modes in the circuit QED microwave cavity.

As considered in [10], the energy scales ϵ and ω_0 for circuit QED are in the GHz regime, while g , Ω , and ω_n can be on much slower timescales, such as in the MHz regime. The modulation rate of the phases $\dot{\theta}_{\pm}(\tau)$ can be expressed in terms of the simulated time-dependent acceleration $a(\tau)$ as [using

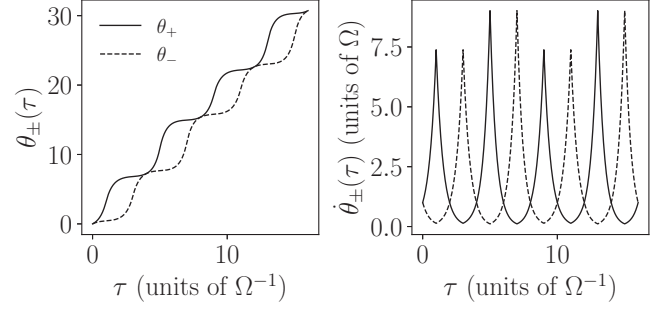


FIG. 3. The phase modulations $\theta_{\pm}(\tau)$ (left panel) and the corresponding rates $\dot{\theta}_{\pm}(\tau)$ that provide the desired simulation of the accelerated motion, where $\Omega = 1$ MHz. Note that modulation rates are in the regime of $\dot{\theta}_{\pm}(\tau) \lesssim 10\Omega = 10$ MHz.

the world line in Eq. (B5)]

$$\begin{aligned} \dot{\theta}_{\pm}(\tau) &= \frac{d}{d\tau} [\omega_n t(\tau) \pm k_n x(\tau)] \\ &= \omega_n \cosh[\xi(\tau)] \pm k_n \sinh[\xi(\tau)] \\ &= \omega_n \cosh \left[\int_0^\tau d\tau' a(\tau') \right] \pm k_n \sinh \left[\int_0^\tau d\tau' a(\tau') \right]. \end{aligned} \quad (\text{C7})$$

Let us consider a typical world line studied in the main text, for example with $a_0 = 2$, $\Delta a/a_0 = 0.1$, $T = 2$, and $\omega_n = \Omega$ [the values used in Fig. 2(f) of the main text] in the units fixed by Ω . Then, we have $\dot{\theta}_{\pm}(\tau) \lesssim 10\Omega$, meaning that the phases in the driving (C3) need to be modulated at roughly the same timescale as Ω , in the MHz band, which is much slower than the circuit QED timescales and should be experimentally feasible.

Finally, let us consider a concrete example of typical parameter values of the analog circuit QED system. Let the parameters of the system be $\omega_0 = 1$ GHz, $\epsilon = 1.1$ GHz, $\Omega = 1$ MHz, $g = 10/\sqrt{3\pi}$ MHz $\simeq 3.3$ MHz, $\eta = 0.01$. The driving frequencies are then $\omega_+ = 2.099$ GHz and $\omega_- = 0.099$ GHz. This simulates the harmonic detector coupled to the $n = 3$ mode of the quantum field (with $\Omega = \omega_n = k_n$ and

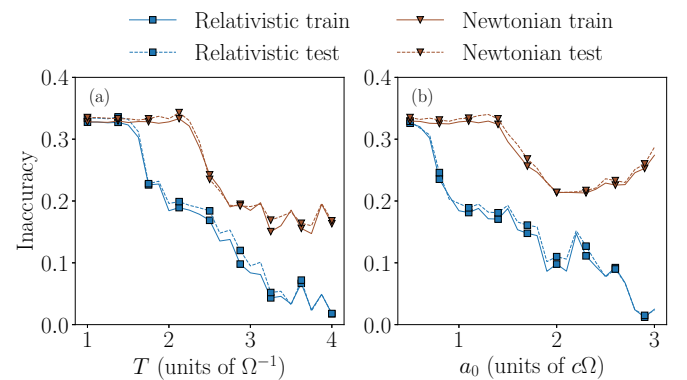


FIG. 4. Performances of the reservoir-computing model considered in the main text, but with a qubit replacing the harmonic oscillator. Same parameters as Figs. 2(d) and 2(e) in the main text, respectively, showing very similar results.

$\lambda = 0.1$) as considered in the main text. To simulate the acceleration sequence described in the main text in the case of $a_0 = 2$, $\Delta a/a_0 = 0.1$, and $T = 2$, the required phase modulations $\theta_{\pm}(\tau)$ as well as their rates $\dot{\theta}(\tau)$, given by Eq. (C7), are plotted in Fig. 3.

APPENDIX D: RESULTS WITH A QUBIT INSTEAD OF A HARMONIC OSCILLATOR

We report here the simulation results when we replace the harmonic detector with a qubit (a two-level atom initially in its ground state) for the same parameters considered in the main text. To model the configuration with the qubit, we have to replace the bosonic mode operator \hat{b} with the Pauli operator $\hat{\sigma}^-$ in the Hamiltonian. Since the Gaussian formalism can no longer be applied, we assumed a single-mode approximation for the quantum field (considering only the mode that is

initially in the coherent state and in resonance with the proper frequency of the qubit), which matches the exact form of the single-mode circuit-QED Hamiltonian in Eq. (C6). The feature vector now contains the expectation values of the operators that are respectively analogous to the bosonic occupation number and the quadratures, namely $\hat{\sigma}^+\hat{\sigma}^-$, $(\hat{\sigma}^- + \hat{\sigma}^+)/\sqrt{2}$, and $i(\hat{\sigma}^+ - \hat{\sigma}^-)/\sqrt{2}$. This is equivalent to measuring the Pauli operators $\hat{\sigma}^z$, $\hat{\sigma}^x$, and $\hat{\sigma}^y$ respectively. The equivalent of Figs. 2(d) and 2(e) in the main text are presented in Figs. 4(a) and 4(b) for the qubit model. We recover results similar to the case of the harmonic detector. Note that the Newtonian model has a slightly improved yet still very poor performance, which can be ascribed to the additional nonlinearity provided by the qubit. These results clearly show that the details of the spectrum of the detector are not crucial for the expressive power of the relativistic quantum dynamics.

-
- [1] A. Peres and D. R. Terno, Quantum information and relativity theory, *Rev. Mod. Phys.* **76**, 93 (2004).
- [2] R. B. Mann and T. C. Ralph, Relativistic quantum information, *Class. Quantum Grav.* **29**, 220301 (2012).
- [3] D. E. Bruschi, C. Sabín, P. Kok, G. Johansson, P. Delsing, and I. Fuentes, Towards universal quantum computation through relativistic motion, *Sci. Rep.* **6**, 18349 (2016).
- [4] D. E. Bruschi, A. Dragan, A. R. Lee, I. Fuentes, and J. Louko, Relativistic Motion Generates Quantum Gates and Entanglement Resonances, *Phys. Rev. Lett.* **111**, 090504 (2013).
- [5] D. E. Bruschi, J. Louko, D. Faccio, and I. Fuentes, Mode-mixing quantum gates and entanglement without particle creation in periodically accelerated cavities, *New J. Phys.* **15**, 073052 (2013).
- [6] N. Friis, M. Huber, I. Fuentes, and D. E. Bruschi, Quantum gates and multipartite entanglement resonances realized by nonuniform cavity motion, *Phys. Rev. D* **86**, 105003 (2012).
- [7] S. L. Braunstein and P. van Loock, Quantum information with continuous variables, *Rev. Mod. Phys.* **77**, 513 (2005).
- [8] E. Martín-Martínez, D. Aasen, and A. Kempf, Processing Quantum Information with Relativistic Motion of Atoms, *Phys. Rev. Lett.* **110**, 160501 (2013).
- [9] J. R. Johansson, G. Johansson, C. M. Wilson, and F. Nori, Dynamical Casimir Effect in a Superconducting Coplanar Waveguide, *Phys. Rev. Lett.* **103**, 147003 (2009).
- [10] M. del Rey, D. Porras, and E. Martín-Martínez, Simulating accelerated atoms coupled to a quantum field, *Phys. Rev. A* **85**, 022511 (2012).
- [11] S. Felicetti, C. Sabín, I. Fuentes, L. Lamata, G. Romero, and E. Solano, Relativistic motion with superconducting qubits, *Phys. Rev. B* **92**, 064501 (2015).
- [12] A. Blais, A. L. Grimsmo, S. M. Girvin, and A. Wallraff, Circuit quantum electrodynamics, *Rev. Mod. Phys.* **93**, 025005 (2021).
- [13] L.-M. Duan and C. Monroe, *Colloquium*: Quantum networks with trapped ions, *Rev. Mod. Phys.* **82**, 1209 (2010).
- [14] G. Tanaka, T. Yamane, J. B. Héroux, R. Nakane, N. Kanazawa, S. Takeda, H. Numata, D. Nakano, and A. Hirose, Recent advances in physical reservoir computing: A review, *Neural Networks* **115**, 100 (2019).
- [15] Guy Van der Sande, D. Brunner, and M. C. Soriano, Advances in photonic reservoir computing, *Nanophotonics* **6**, 561 (2017).
- [16] S. Sunada, K. Kanno, and A. Uchida, Using multidimensional speckle dynamics for high-speed, large-scale, parallel photonic computing, *Opt. Express* **28**, 30349 (2020).
- [17] D. Pierangeli, G. Marcucci, and C. Conti, Photonic extreme learning machine by free-space optical propagation, *Photon. Res.* **9**, 1446 (2021).
- [18] K. Vandoorne, P. Mechet, T. Van Vaerenbergh, M. Fiers, G. Morthier, D. Verstraeten, B. Schrauwen, J. Dambre, and P. Bienstman, Experimental demonstration of reservoir computing on a silicon photonics chip, *Nat. Commun.* **5**, 3541 (2014).
- [19] F. Denis-Le Coarer, M. Sciamanna, A. Katumba, M. Freiburger, J. Dambre, P. Bienstman, and D. Rontani, All-optical reservoir computing on a photonic chip using silicon-based ring resonators, *IEEE J. Sel. Top. Quantum Electron.* **24**, 1 (2018).
- [20] A. Opala, S. Ghosh, T. C. H. Liew, and M. Matuszewski, Neuromorphic Computing in Ginzburg-Landau Polariton-Lattice Systems, *Phys. Rev. Appl.* **11**, 064029 (2019).
- [21] D. Ballarini, A. Gianfrate, R. Panico, A. Opala, S. Ghosh, L. Dominici, V. Ardizzone, M. De Giorgi, G. Lerario, G. Gigli, T. C. H. Liew, M. Matuszewski, and D. Sanvitto, Polaritonic neuromorphic computing outperforms linear classifiers, *Nano Lett.* **20**, 3506 (2020).
- [22] R. Mirek, A. Opala, P. Comaron, M. Furman, M. Król, K. Tyszka, B. Sereďyński, D. Ballarini, D. Sanvitto, T. C. H. Liew, W. Pacuski, J. Suffczyński, J. Szczytko, M. Matuszewski, and B. Piętko, Neuromorphic binarized polariton networks, *Nano Lett.* **21**, 3715 (2021).
- [23] M. S. Kulkarni and C. Teuscher, Memristor-based reservoir computing, in *Proceedings of the 2012 IEEE/ACM International Symposium on Nanoscale Architectures (NANOARCH)* (ACM, 2012), pp. 226–232.
- [24] C. Du, F. Cai, M. A. Zidan, W. Ma, S. H. Lee, and W. D. Lu, Reservoir computing using dynamic memristors for temporal information processing, *Nat. Commun.* **8**, 2204 (2017).

- [25] S. Boyn, J. Grollier, G. Lecerf, B. Xu, N. Locatelli, S. Fusil, S. Girod, C. Carrétero, K. Garcia, S. Xavier, J. Tomas, L. Bellaiche, M. Bibes, A. Barthélémy, S. Saïghi, and V. Garcia, Learning through ferroelectric domain dynamics in solid-state synapses, *Nat. Commun.* **8**, 14736 (2017).
- [26] R. Nakane, G. Tanaka, and A. Hirose, Reservoir computing with spin waves excited in a garnet film, *IEEE Access* **6**, 4462 (2018).
- [27] D. Marković, N. Leroux, M. Riou, F. Abreu Araujo, J. Torrejon, D. Querlioz, A. Fukushima, S. Yuasa, J. Trastoy, P. Bortolotti, and J. Grollier, Reservoir computing with the frequency, phase, and amplitude of spin-torque nano-oscillators, *Appl. Phys. Lett.* **114**, 012409 (2019).
- [28] G. Marcucci, D. Pierangeli, and C. Conti, Theory of Neuromorphic Computing by Waves: Machine Learning by Rogue Waves, Dispersive Shocks, and Solitons, *Phys. Rev. Lett.* **125**, 093901 (2020).
- [29] D. Marković and J. Grollier, Quantum neuromorphic computing, *Appl. Phys. Lett.* **117**, 150501 (2020).
- [30] R. Araiza Bravo, K. Najafi, X. Gao, and S. F. Yelin, Quantum reservoir computing using arrays of Rydberg atoms, *PRX Quantum* **3**, 030325 (2022).
- [31] S. Ghosh, A. Opala, M. Matuszewski, T. Paterek, and T. C. H. Liew, Quantum reservoir processing, *npj Quantum Inf.* **5**, 35 (2019).
- [32] S. Ghosh, A. Opala, M. Matuszewski, T. Paterek, and T. C. H. Liew, Reconstructing quantum states with quantum reservoir networks, *IEEE Trans. Neural Netw. Learn. Syst.* **32**, 3148 (2020).
- [33] S. Ghosh, T. Paterek, and T. C. H. Liew, Quantum Neuromorphic Platform for Quantum State Preparation, *Phys. Rev. Lett.* **123**, 260404 (2019).
- [34] S. Ghosh, T. Krisnanda, T. Paterek, and T. C. H. Liew, Realising and compressing quantum circuits with quantum reservoir computing, *Commun. Phys.* **4**, 105 (2021).
- [35] T. Krisnanda, S. Ghosh, T. Paterek, and T. C. H. Liew, Creating and concentrating quantum resource states in noisy environments using a quantum neural network, *Neural Networks* **136**, 141 (2021).
- [36] H. Xu, T. Krisnanda, W. Verstraelen, T. C. H. Liew, and S. Ghosh, Superpolynomial quantum enhancement in polaritonic neuromorphic computing, *Phys. Rev. B* **103**, 195302 (2021).
- [37] V. Heyraud, Z. Li, Z. Denis, A. Le Boité, and C. Ciuti, Noisy quantum kernel machines, [arXiv:2204.12192](https://arxiv.org/abs/2204.12192).
- [38] J. Dong, M. Rafayelyan, F. Krzakala, and S. Gigan, Optical reservoir computing using multiple light scattering for chaotic systems prediction, *IEEE J. Sel. Top. Quantum Electron.* **26**, 1 (2020).
- [39] M. Rafayelyan, J. Dong, Y. Tan, F. Krzakala, and S. Gigan, Large-Scale Optical Reservoir Computing for Spatiotemporal Chaotic Systems Prediction, *Phys. Rev. X* **10**, 041037 (2020).
- [40] A. Saade, F. Caltagirone, I. Carron, L. Daudet, A. Dreameau, S. Gigan, and F. Krzakala, Random projections through multiple optical scattering: Approximating Kernels at the speed of light, in *Proceedings of the 2016 IEEE International Conference on Acoustics, Speech, and Signal Processing (ICASSP)* (IEEE, New York, 2016).
- [41] R. Ohana, J. Wacker, J. Dong, S. Marmin, F. Krzakala, M. Filippone, and L. Daudet, Kernel Computations from Large-Scale Random Features Obtained by Optical Processing Units, in *Proceedings of the ICASSP 2020 IEEE International Conference on Acoustics, Speech, and Signal Processing (ICASSP)* (IEEE, New York, 2020), pp. 9294–9298.
- [42] Z. Denis, I. Favero, and C. Ciuti, Photonic Kernel Machine Learning for Ultrafast Spectral Analysis, *Phys. Rev. Appl.* **17**, 034077 (2022).
- [43] E. G. Brown, E. Martín-Martínez, N. C. Menicucci, and R. B. Mann, Detectors for probing relativistic quantum physics beyond perturbation theory, *Phys. Rev. D* **87**, 084062 (2013).
- [44] W. G. Unruh and R. M. Wald, What happens when an accelerating observer detects a rindler particle, *Phys. Rev. D* **29**, 1047 (1984).
- [45] A. Ahmadzadegan, R. B. Mann, and E. Martín-Martínez, Measuring motion through relativistic quantum effects, *Phys. Rev. A* **90**, 062107 (2014).
- [46] N. D. Birrell and P. C. W. Davies, *Quantum Fields in Curved Space*, Cambridge Monographs on Mathematical Physics (Cambridge University, Cambridge, England, 1982).
- [47] M. O. Scully and M. S. Zubairy, *Quantum Optics* (Cambridge University, New York, 1997).
- [48] B. Šoda, V. Sudhir, and A. Kempf, Acceleration-Induced Effects in Stimulated Light-Matter Interactions, *Phys. Rev. Lett.* **128**, 163603 (2022).
- [49] Defined as the eigenstate of the annihilation operator \hat{a}_i with eigenvalue α , i.e. $\hat{a}_i|\alpha_{\omega_i}\rangle = \alpha|\alpha_{\omega_i}\rangle$ [47].
- [50] R. Simon, E. C. G. Sudarshan, and N. Mukunda, Gaussian pure states in quantum mechanics and the symplectic group, *Phys. Rev. A* **37**, 3028 (1988).
- [51] C. Weedbrook, S. Pirandola, R. García-Patrón, N. J. Cerf, T. C. Ralph, J. H. Shapiro, and S. Lloyd, Gaussian quantum information, *Rev. Mod. Phys.* **84**, 621 (2012).
- [52] G. Adesso, S. Ragy, and A. R. Lee, Continuous variable quantum information: Gaussian states and beyond, *Open Syst. Inf. Dyn.* **21**, 1440001 (2014).
- [53] The anharmonicity of a Josephson atom can be made arbitrarily small by replacing a junction by a chain of junctions, as the anharmonicity scales as $1/N^2$ where N is the number of junctions.
- [54] D. E. Bruschi, J. Louko, E. Martín-Martínez, A. Dragan, and I. Fuentes, Unruh effect in quantum information beyond the single-mode approximation, *Phys. Rev. A* **82**, 042332 (2010).
- [55] R. Kuzmin, N. Mehta, N. Grabon, R. Mencia, and V. E. Manucharyan, Superstrong coupling in circuit quantum electrodynamics, *npj Quantum Inf.* **5**, 1 (2019).
- [56] J. Puertas Martínez, S. Léger, N. Gheeraert, R. Dassonneville, L. Planat, F. Foroughi, Y. Krupko, O. Buisson, C. Naud, W. Hasch-Guichard, S. Florens, I. Snyman, and N. Roch, A tunable Josephson platform to explore many-body quantum optics in circuit-QED, *npj Quantum Inf.* **5**, 1 (2019).
- [57] N. Mehta, R. Kuzmin, C. Ciuti, and V. E. Manucharyan, Down-conversion of a single photon as a probe of many-body localization, [arXiv:2203.17186](https://arxiv.org/abs/2203.17186).
- [58] S. Vriend, D. Grimmer, and E. Martín-Martínez, The unruh effect in slow motion, *Symmetry* **13**, 1977 (2021).
- [59] W. Rindler, *Introduction to Special Relativity* (Clarendon, Oxford, 1982).
- [60] We assume ensemble measurements for the quantum expectation values.

- [61] D. Grimmer, I. Melgarejo-Lermas, and E. Martin-Martinez, Machine learning quantum field theory with local probes, [arXiv:1910.03637](https://arxiv.org/abs/1910.03637).
- [62] K. Lang, Learning to tell two spiral apart, in *Proceedings of the 1988 Connectionist Models Summer School* (ResearchGate, Berlin, Germany, 1989), pp. 52–59.
- [63] C.-C. Yu and B.-D. Liu, A backpropagation algorithm with adaptive learning rate and momentum coefficient, in *Proceedings of the 2002 International Joint Conference on Neural Networks*, IEEE Conf. Proc. No. 02CH37290 (IEEE, New York, 2002).
- [64] T. Hastie, R. Tibshirani, and J. Friedman, *The Elements of Statistical Learning: Data Mining, Inference, and Prediction* (Springer, New York, 2013).
- [65] With respect to the inner product on L^2_μ : $\langle f, h \rangle \equiv \int f(\mathbf{x})h(\mathbf{x})\mu(d\mathbf{x})$, where $\mu(d\mathbf{x})$ denotes the probability measure of the samples.
- [66] V. I. Paulsen and M. Raghupathi, *An Introduction to the Theory of Reproducing Kernel Hilbert Spaces*, Cambridge Studies in Advanced Mathematics (Cambridge University, Cambridge, England, 2016).
- [67] The space of square-integrable functions with respect to the probability measure of the input distribution $\mu(d\mathbf{x})$.
- [68] C. Williams and M. Seeger, Using the Nyström method to speed up kernel machines, in *Advances in Neural Information Processing Systems 13* (MIT, Cambridge, MA, 2001), pp. 682–688.
- [69] This is to ensure that the cavity is long enough for the atom to remain inside. For the circuit QED implementation this is not an important detail.
- [70] I. Goodfellow, Y. Bengio, and A. Courville, in *Deep Learning*, edited by F. Bach, Adaptive Computation and Machine Learning Series (MIT, Cambridge, MA, 2016).
- [71] Note that our driving term is different from that in [10], as they considered simulating a quantum field in free space, while in the present paper the simulated quantum field is confined within a cavity with Dirichlet boundary conditions, resulting in different mode functions.